3D-printed Origami Packaging with Inkjet-printed Antennas for RF Harvesting Sensors

John Kimionis, *Student Member, IEEE*, Michael Isakov, Apostolos Georgiadis, *Senior Member, IEEE*,
Beom S. Koh, and Manos M. Tentzeris, *Fellow, IEEE*

Abstract—This paper demonstrates the combination of additive manufacturing techniques for realizing complex 3D origami structures for high frequency applications. A 3D-printed compact package for enclosing radio frequency (RF) electronics is built, that features on-package antennas for RF signal reception (for harvesting or communication) at orthogonal orientations. Conventional 3D printing technologies often require significant amounts of time and supporting material to realize certain structures, such as hollow packages. In this work, instead of fabricating the package in its final 3D form, it is 3D-printed as a planar structure with "smart" shape-memory hinges that allow origami folding to a 3D shape after heating. This significantly reduces fabrication time and effectively eliminates the need for supporting material, thus minimizing the overall manufacturing cost. Metallization on the package is performed by directly inkjet printing conductive inks on top of the 3D-printed surface with a modified inkjet-printed process without the need for surface treatment or processing. Inkjet-printed on-package conductive features are successfully fabricated, that are combined with RF energy harvesting electronics to showcase the proof-of-concept of utilizing origami techniques to build fully 3D RF systems. The methodologies presented in this paper will be enabling the manufacturing of numerous real-time shape-changing 3D complex structures for electromagnetic applications.

Index Terms—additive manufacturing, origami electronics, 3D printing, inkjet printing, RF harvesting

I. INTRODUCTION

Low-cost and low-power connectivity is a necessity for large-scale wireless sensor networks (WSNs). Power sufficiency is one of the most important challenges in the practical WSN designs, and radio frequency (RF) energy harvesting gradually proves that it is an enabling technology for demanding low-power applications. The need for the manual battery replacement can be potentially eliminated by utilizing RF harvesting for autonomous sensor operation, or for automatic battery recharging on-site [1], [2].

J. Kimionis, B. S. Koh, and M. M. Tentzeris are with the School of Electrical and Computer Engineering, Georgia Institute of Technology, Atlanta, Georgia, USA, 30332-0250. A. Georgiadis is with Centre Tecnologic de Telecommunicacions de Catalunya, Castelldefels 08860, Spain. M. Isakov is with the School of Mechanical Engineering, Georgia Institute of Technology, Atlanta, Georgia, USA, 30332-0250. Email:{ikimionis@gatech.edu, misakov3@gatech.edu, ageorgiadis@cttc.es, bkoh6@gatech.edu, etentze@ece.gatech.edu}.
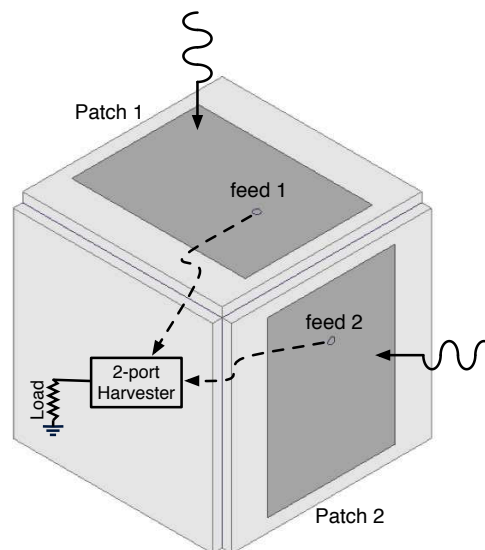
Fig. 1. 3D cube with orthogonally-positioned on-side planar antennas on the sides and enclosed RF energy harvesting electronics.

There have been numerous efforts related to rectenna design, such as for example ones addressing multiband operation [3]–[5]. Also, a large amount of power rectenna arrays have been considered [6]–[8]with broadband, dual band, circular or linear polarization characteristics. One of the challenges in designing rectenna arrays has been the trade-off between combining the output of the individual antenna elements in RF forming directive antenna arrays or in DC forming non-directive rectifier arrays. The combination in RF results in directive systems able to focus towards a specific transmitter.

In this work, we mainly consider large-scale systems in outdoor or indoor scenarios for "smart" sensors, energy harvesters, or communicators that require an easy deployment, e.g. spreading sensors with random orientation within a large area, and a compact "rugged" packaging. In such random deployment scenarios, communication or harvesting might be compromised if the node's antenna does not face to the direction of the central station for conveying data or receiving power wirelessly. Conventionally, most WSN nodes employ either wire monopole/dipole antennas, or planar patch antennas. In both cases, the direction of maximum directivity is mainly limited to one dimension. Employing novel fully 3D structures, such as a cube, allows for the easy placement of (planar) antennas on multiple faces, enabling simultaneous harvesting/communication over different and potentially real-

time reconfiguring (e.g. "origami") orientations (Fig. 1). RF waves from totally orthogonal planes can be exploited for harvesting and backscatter communication, enhancing the total system efficiency when multiple sources/gateways are present. Such a system can also benefit in the case of a single source that lies in an unknown direction: two orthogonal antennas increase the probability of capturing the source-emitted plane waves, compared to a single antenna facing to a single direction that can only capture RF signals from multipath reflections.

Hosting the node's antennas directly *on* the package reduces the total volume that would be required if monopole/dipole wire antennas stemming out of the package were utilized. Mechanical damage (e.g. breaking) of antennas can also be minimized since the antennas are a part of the package in this case.

In this paper, a system design is presented that will benefit WSN nodes in terms of harvesting and, possibly, communication: All electronics of the WSN nodes reside inside fully 3D enclosures, in this case a cube, that can be easily deployed on a field. Exposing only the antennas to the outer world and placing all the electronics inside the package makes the node compact, and facilitates deployment.

For the fabrication of the package and its antennas, an all-additive manufacturing process is followed to facilitate prototyping and minimize the need for post-processing (e.g. connecting individual cube sides with adhesives). 3D printing is chosen for creating the plastic outer shell of the system that will a) enclose the electronics and b) host the antennas. Fabricating a cube is a straightforward process with most 3D printers; however, three main challenges appear for a packaging "smart cube" that will be used in this application:

1) The cube must be hollow, to allow for the easy and rugged placement of electronics in its interior. This typically requires the use of a supporting material that has to be removed after fabrication. For a moderately large cube size (in order to fit printed circuit boards, cables, batteries, etc) the cost of the supporting material often becomes more significant than the cost of the material used for the actual cube.

2) The fabrication time for a 3D structure is mainly limited by its exterior volume. For the cube size required for the proof-of-concept structures of this paper ($2 \sim 2.5$ inch edges), the long fabrication time slows down the prototyping process.

3) The cube must have a way to open/close - preferably in real time - at least one of the sides for placing/replacing electronics in its interior.

The aforementioned challenges cannot be directly addressed with typical 3D printing techniques, and demand a non-conventional approach for the fabrication of complex 3D structures, especially with operability up to the RF frequency range. Inspired by the art of Origami folding to build multiple 3D shapes from miniaturized planar (2D) structures, in this paper we introduce novel origami-based concepts as the foundation for the additive manufacturing of real-time shape-changing 3D complex structures targeting high frequency electromagnetic applications.
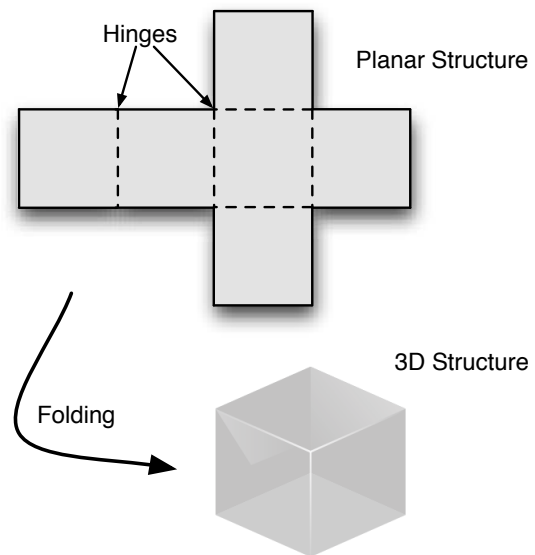

Fig. 2. Origami folding of planar structure to realize a 3D shape.

Specifically, origami folding is the technique chosen to overcome the long fabrication time and high fabrication cost limitations by "folding" a two-dimensional structure to a three-dimensional one. The original 2D structure can be either a thin easily-foldable substrate, such as paper, a 3D-printed structure made of flexible polymer, or a hard 3D-printed "thick" planar structure with "hinging" features that allow folding [9]. The latter has the advantage of mechanical stability which is important for packaging scenarios, e.g. protecting electronics inside the origami package.

The implementation of an origami electromagnetic structure involves two phases. During the first phase, it is designed and simulated in its final 3-dimensional form. The design is optimized to achieve the desired operating performance (e.g. operating frequency), which, apart from the materials and dimensions, also highly depends on the structure geometry. The second phase involves 'unfolding' the structure to a 2-dimensional pattern that can be easily fabricated. In the case of a cube, it can be expanded to a cross-shaped planar form, shown in Fig. 2-top. If the cube has dimensions $a \times a \times a$ and a thickness of $b << a$, the fabrication time for a 3D cube is limited by its exterior volume

$$V_{\text{cube}} = (a + 2b)^3,$$

while for the cross shape it is

$$V_{\text{cross}} = 6 \times (a \times a \times b),$$

which is 1 order of magnitude smaller compared to the cube. Thus, the fabrication time can be significantly reduced, and the need for supporting material can be effectively eliminated.

For the metallization of the 3D-printed structure in an additive manufacturing manner, inkjet printing can be utilized. Inkjet printing has proven to be a successful process for realizing low-cost high-frequency structures accurately on a plethora of different substrates, including flexible ones [10]. Printing on 3D-printed surfaces for high frequency sensing and harvesting
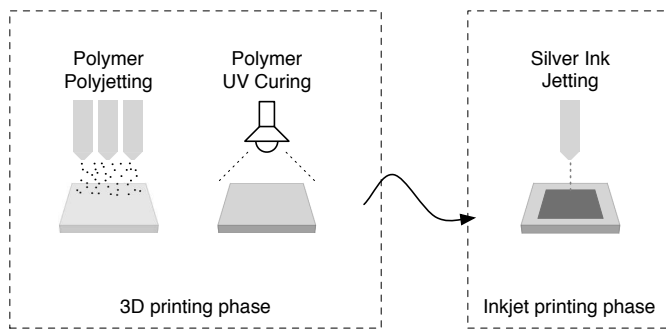
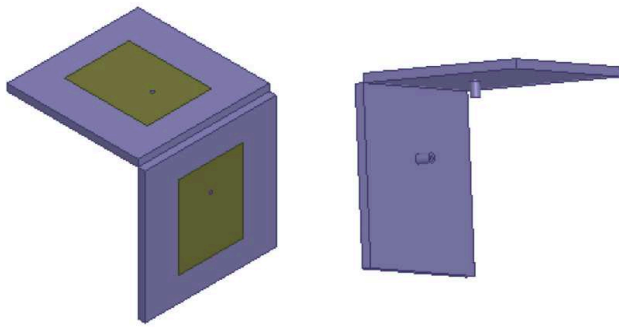Fig. 3. All-additive manufacturing: 3D printing of substrate and inkjet printing of conductive features.

Fig. 4. Partial views of the package exterior (left) and interior (right).

applications has been demonstrated in [11], showing promising results, even on challenging, rough surfaces.

The combination of 3D printing and inkjet printing can greatly facilitate rapid prototyping, as both are fully additive processes. A significant advantage of this combination is that no post-processing is required after the 3D printing phase to start the inkjet-printing phase. In principle, the two processes could be combined in the same piece of equipment capable of performing a sequence of 3D material deposition and jetting of conductive, semiconductive, or dielectric inks (Fig. 3).

II. PACKAGING DESIGN

For proof-of-concept purposes, a cubic-shape packaging structure prototype has been designed in its final 3D form and has been modeled with the ANSYS High Frequency Structure Simulation (HFSS) software to analyze the performance of its electromagnetic features in high frequencies ($2 \sim 2.6$ GHz band). Since the electronics are contained within the cube, probe-fed patches have been selected as the on-package antennas with coaxial connectors in the interior of the cube. The patches are implemented with microstrip technology, printed on the external sides of the cube, while employing metal ground planes on the respective interior sides. The directivity of patch antennas due to the ground plane limits the electromagnetic coupling between the antennas and the electronics inside the cube. Two patches have been designed on two sides of the cube, so that they face to orthogonal directions (Fig. 4).

The cube sides are 5.7×5.7 cm squares and are 3 mm thick. On two of the cube sides patch antennas have been designed
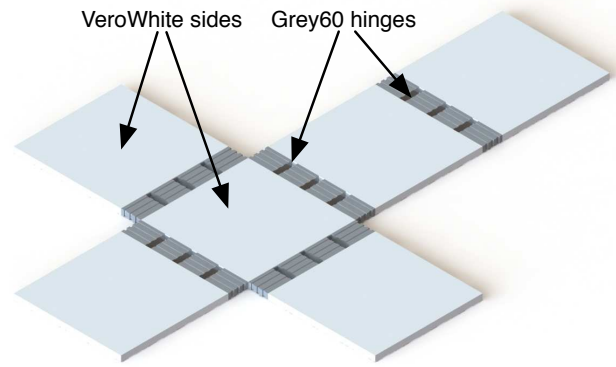

Fig. 5. Rendering of the flat configuration of the folding package used for 3D printing.

around the central frequency of 2.3 GHz. The patch width is $W = 2.79$ cm and its length is $L = 3.59$ cm. The probe feeding point resides 0.63 cm away from the center of the patch, along the L dimension.

Apart from the full 3D structure, a single patch on a substrate with the same dimensions as one cube's side has been simulated. The performance of the single patch and the patches on the cube has been similar, i.e. there are no significant coupling effects between the two antennas on the cube's sides that would degrade their performance (tuning/gain). In principle, an antenna could be placed on any side of the cube without a significant effect on the other sides' antennas.

It is important to note that since the feeding terminals of the two antennas are separate (no RF combining) and the two antennas show a high isolation, their operation is expected to be orthogonal in terms of radiation pattern directivity. In contrast, if the two antennas utilized a common feeding point or if there was a strong coupling, the result would be a beam steering at the far field which would not be desired for the multi-direction operation of the system in Fig. 1.

III. 3D & INKJET ORIGAMI MANUFACTURING

A 3D-printed packaging prototype has been fabricated using an Objet Connex 260 3D Polyjet Printer. The structural surfaces of the cube are made of the proprietary material VeroWhite and the hinges are Grey60, both thermoset shape memory polymers (SMP). The cube has been printed in its flat configuration to simplify the manual folding process, minimize material consumption, and reduce turnaround time. The model, which has been designed in SolidWorks and is shown in Fig. 5, has been printed diagonally on the printer bed to accommodate for the big length across its longest dimension (Fig. 6). The materials for printing were chosen to maximize part strength and minimize the required temperature for folding. A novel hinge design has also been employed to reduce material fracture during the manual folding process after heating it up.

Shape memory polymers (SMPs) are polymers that can programmatically change shape "on-demand" [12]. Typically, an SMP is manually folded from an initial primary shape to a secondary shape by applying a mechanical load above the
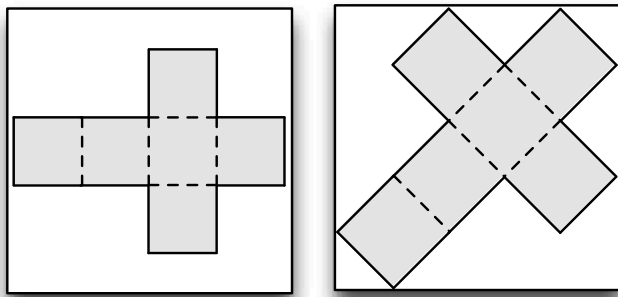
Fig. 6. Exploitation of the full 3D printer bed for building longer-dimension structures.

Fig. 7. DMA (Dynamic Mechanical Analysis) of Grey60 yielding T_g of $55°C$.

Fig. 8. Shape recovery ratio vs. time for Grey60.

glass transition temperature T_g. The SMP will maintain this deformed shape after subsequently lowering the temperature below T_g and removing the externally-applied mechanical load. Upon reheating above T_g from the secondary shape, the SMP will self-fold and recover its primary shape [12]. Shape memory polymers recover at different rates (a measure of the shape recovery ratio with respect to time) and at different temperatures (T_g), so material selection is a key design step in achieving desired properties during self-folding. In the case of the folding package designed in this paper, the primary shape is the flat printed configuration and the secondary shape is the manually-folded configuration. For $90°$ folding, the final shape is a box, while different shapes may result from arbitrary folding angles.

The mechanical properties for the hinge material chosen in designing the folding box are shown in Fig. 7. The hinges and structural surfaces of the box have been selected to be as stiff as possible amongst the available Objet materials for part strength. The structural material has been chosen to have a significantly higher T_g than the hinge material to eliminate undesired deformations during heating. The low T_g of the hinge material has also been chosen to reduce the ambient environmental impact on the assembled device during heating and cooling cycles. The T_g was determined using a Dynamic Mechanical Analyzer (DMA, TA Instruments, Model Q800) and examining the $\tan(\delta)$ (ratio of loss modulus to storage modulus).[1] For Grey60, the T_g is $55°C$. For VeroWhite, the T_g is $70°C$ and the Young's modulus is 1.2 GPa [9], [13]. The recovery rate is important only for the actuating material and is approximately 2.5 seconds for 100% recovery.

Transitioning from the flat primary shape to the cube shape is generally achieved by heating and subsequently manually deforming the part by hand. This process subjects the hinges of the folding box to irregular and random stress patterns, increasing the likelihood of part failure. To improve the damage tolerance during folding a periodic step profile was employed along the surface contour of the hinge (Fig. 9). Thinner stepwise sections require lower bending stress and have higher thermal conductivity, making the folding box both

[1]Not to be confused with the dielectric loss $\tan \delta$. Storage modulus: measure of elastic energy of material or energy stored during sinusoidal stretching. Loss modulus: measure of viscous energy of material or energy dissipated as heat during sinusoidal stretching.
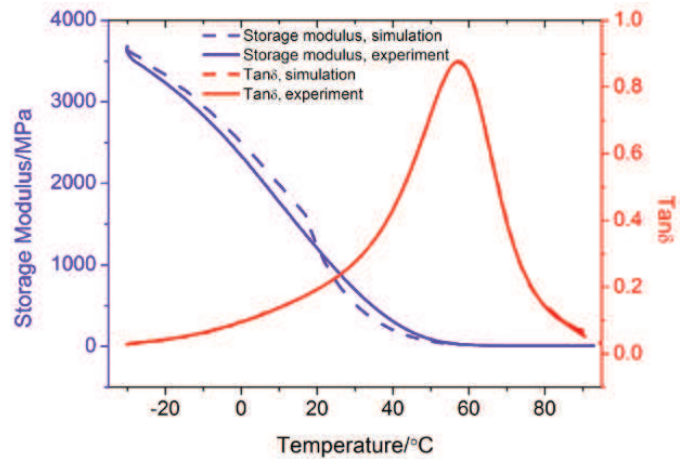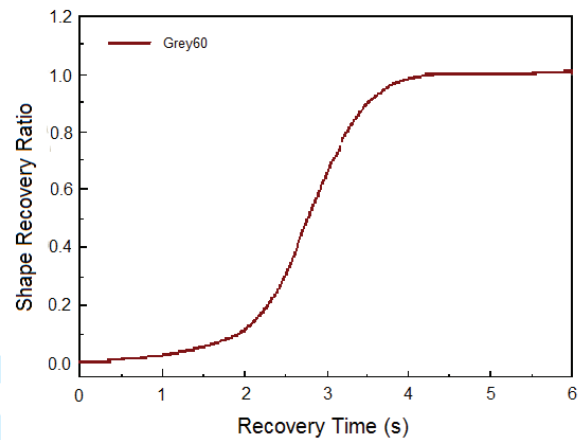
easier and faster to fold. Additionally, the periodic profile allows for a wider range of bending motion during folding since the hinge is not subject to restrictive compressive strains. The hinges feature slots to form independent bending sections along themselves and improve their longevity in case of minor fractures (Fig. 9). The hinge radius has been maximized to further simplify the manual folding process. Given the dimensional constraints of the structural faces of the folding box and the build volume of the Objet Connex 3D Inkjet Printer, the highest achievable bend radius of 10.5 mm was chosen.

The main challenge for the effective metallization (to realize transmission lines, printed circuits, or antennas) is the direct inkjet printing of conductive features on the 3D-printed surface before folding. This is advantageous for the simplification of the fabrication process:

1) No post-processing is required, such as surface treatment between the 3D and inkjet printing phases, or use of dielectric layers to smooth the surface before metallization. This is in contrast with inkjet printing on top of silicon integrated circuits (ICs), where the printing of supporting layers is required [14].
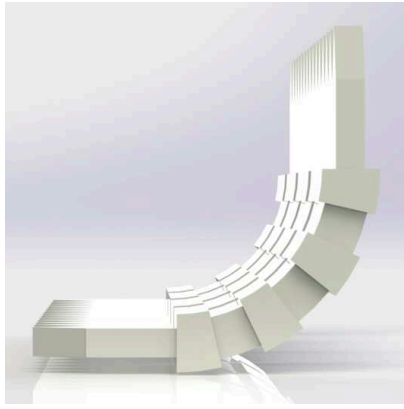
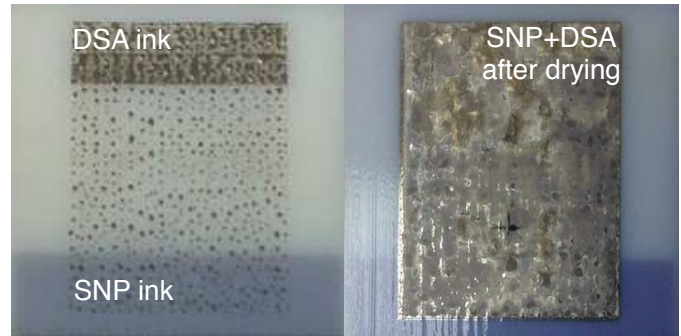Fig. 9. Rendering of the hinge design in a $90°$ folded orientation.

Fig. 10. Left: Silver nanoparticle (SNP) ink layer with partial diamminesilver acetate (DSA) ink layer on top. Right: SNP+DSA patch after heat drying.

2) Inkjet printing while the structure is still in planar form facilitates and further simplifies printing; the conductive ink drops are deposited vertically in a conventional inkjet printing manner and no high-pressure aerosol jetting techniques are required. Moreover, the thickness of the planar structure (on the order of millimeters) allows for the easy placement of the substrate between the printing bed and printing head; most inkjet printers are limited on the maximum height of the print head since they are mainly designed to accommodate thin substrates and not high 3D structures.

It has to be stressed that the 2D inkjet printing process, that has been widely used for the printing of nanoparticle-based (e.g. silver nanoparticle-SNP, dielectrics, carbon nanotube) inks on photo paper, polyimide films, glass, and other substrates, has to be redefined to address the two main challenges regarding 3D-printed surfaces

- 3D-printed surfaces show extensive surface roughness that results in the formation of non-continuous features for a small number of SNP layers. This results in non-conductive or low-conductivity printed features, due to the discrete drop formation.
- Typically, SNP inks need to be sintered at temperatures higher than $120°$ C to maximize conductivity. However, high temperature levels cannot be tolerated by commonly utilized 3D-printed plastics or resins, causing deformation of the structure or failure (melting).

The above constraints require a modification of the inkjet printing process, which cannot be based solely on SNP inks for the realization of conductive surfaces.

For the metallization on 3D-printed surfaces, a diamminesilver acetate (DSA) ink is used that achieves high conductivity values with moderate temperature curing (ranging from room temperatures up $100°C$). The low temperature range is safe for plastics, and, thus, this is the principal ink used for the fabrication process. Moreover, the DSA ink does not contain any nanoparticles; the particle formation occurs on the substrate after printing. This results in a very low-viscosity ink that spreads easily on the surface and forms continuous conductors.

To avoid over-spreading of the DSA ink, SNP ink is first printed on the substrate to form the patch area. Two layers of SNP form a mesh of discrete drops that can be seen in Fig. 10-left. Then, the DSA ink is printed on top of the SNP drops. Due to its low viscosity, it fills the gaps between the SNP drops, forming a continuous conductor. Up to twenty layers of DSA are printed, to achieve high conductivity. After each layer printing, moderate heat drying follows to guarantee DSA curing uniformity. After the process consisting of printing the SNP layers and printing/drying the DSA layers is completed, the result is a uniform conductor on top of the 3D-printed surface, without any ink spreading. A fully-cured silver patch can be seen in Fig. 10-right.

To characterize the resistivity of the DSA ink depending on the number of of printed layers, various identical geometry samples have been fabricated with different (5, 10, 15, and 20) layers of DSA, with and without the two SNP layers and the samples' resistivity (in Ω per square) is shown in Fig. 11. It can be seen that for both cases, the first 15 layers are critical for reducing the total resistivity, while the SNP+DSA combination always features a lower resistivity for the same number of DSA layers, compared to the DSA-only case. Although this might be anticipated due to the extra silver content for the SNP+DSA case, it is noted that for the DSA-only structures, more than 5 additional DSA layers are always required to achieve similar resistivity levels with the SNP+DSA structure. This is a significant observation, considering that the SNP layers are not fully cured to maximize their conductivity, since heating temperature is kept at levels below $100°C$.

On top of the fact that the SNP layers lower the resistance of the printed features, it has been concluded from multiple printing experiments that the SNP layers have the advantage of preventing ink "bleeding", and thus the SNP step is always favorable for the fabrication of any structure.

A proof-of-concept patch antenna prototype has been fabricated with 2 SNP layers and 20 DSA layers on a 3D-printed slab that has the same dimensions as the designed cube's sides (5.7×5.7 cm, thickness = 3 mm) for prototyping. On the top side of the slab, the 2.79×3.59 cm patch has been printed, while the bottom side has been covered with adhesive copper tape, to form the ground plane of the antenna for the reason of fabrication simplicity. It is noted that since the ground plane does not require an accuracy of the same level as the patch regarding its dimensions (width, length) or placement (origin
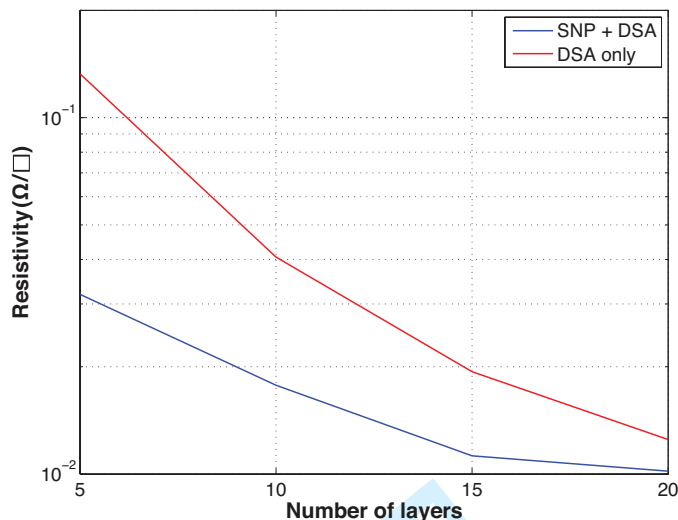
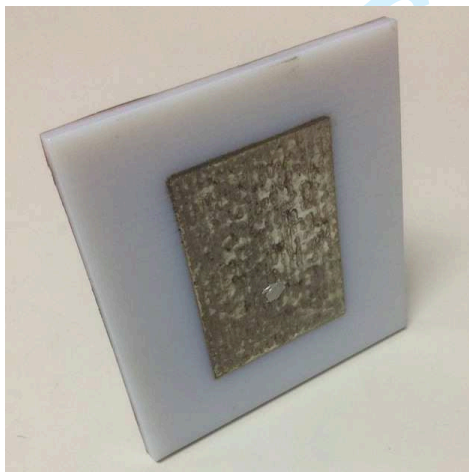Fig. 11. Comparison of resistivity between DSA-only and DSA+SNP metallization.

Fig. 12. Single patch antenna fabricated on 3D-printed substrate.

point), the copper tape is a convenient way to implement it for proof-of-concept purposes. However, silver ink could be used for the ground plane fabrication as well, since it has been previously demonstrated to perform well for ground plane formation, even with meshed designs [15].

A 36 mil hole has been drilled 0.63 cm away from the center of the patch to accommodate the feeding pin. The hole has been drilled with a conventional drill press, and the exact drilling point has been marked by inkjet-printing a fiducial point with black ink after the metallization process. Such a fiducial point can be seen in Fig. 10-right as a black cross. An SMA connector has been mounted and its signal pin has been trimmed to match the height of the antenna plane. A conductive silver epoxy has been used to electrically connect the probe pin to the inkjet-printed silver, and at the same time provide mechanical support for the SMA connector at the backside of the plastic slab.

The same patch antenna has been printed on two orthogonal sides of the cube, to realize the multi-direction harvest-
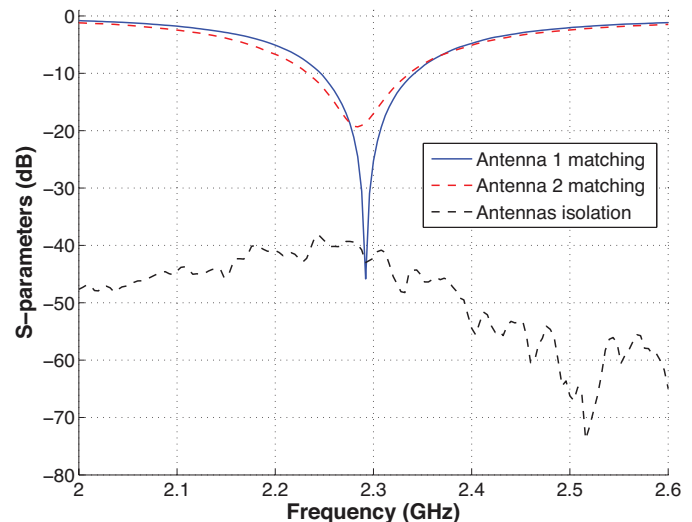

Fig. 13. S-parameters of the 2 patch antennas.

ing/communication system, as shown in Fig. 14-left. The two antennas have been printed with the same process, apart from the drying temperature. For the first antenna, a heatgun with a temperature of approximately $80°$C has been used for 2 minutes, while for the second antenna, the heatgun is set to $50°$C. The different curing temperature is used to assess the effect of the temperature level on the antennas' performance. After the antennas fabrication, the structure is heated and folded to its 3D form (Fig. 14-right).

IV. ANTENNA MEASUREMENTS

The two antennas have been characterized with a vector network analyzer (VNA) as a full 2-port system, rather than two individual antennas. The measured S-parameters are shown in Fig. 13. Both antennas are tuned around 2.3 GHz and exhibit the same -10 dB bandwidth of 100 MHz. It is noted that the first antenna shows a return loss (RL) of less than -40 dB at the resonance frequency, while the second antenna shows a RL of -20 dB. This is attributed to the different heatgun drying temperatures used for the antennas that affects their conductivity; the higher $80°$C temperature visibly benefits the RL. However, it is noted that even the lower temperature of $50°$C is more than sufficient for high conductivity, since 99% of the power exciting the antenna port is delivered to the antenna.

For the two antennas, a strong requirement is the isolation between them to guarantee an orthogonal operation across the frequency band. An isolation of more than 40 dB is achieved between the two fabricated patches (Fig. 13), and thus the effect of each antenna to the other is negligible. This is the combined result of both the geometry of the setup (the antennas are placed in perpendicular planes) and the radiation pattern (directive) of the patches.

The realized gain of each patch antenna has been characterized using a VNA and standard horn antennas in a lab environment. The measured maximum gain across the frequency band is shown in Fig. 15, where is can be seen that
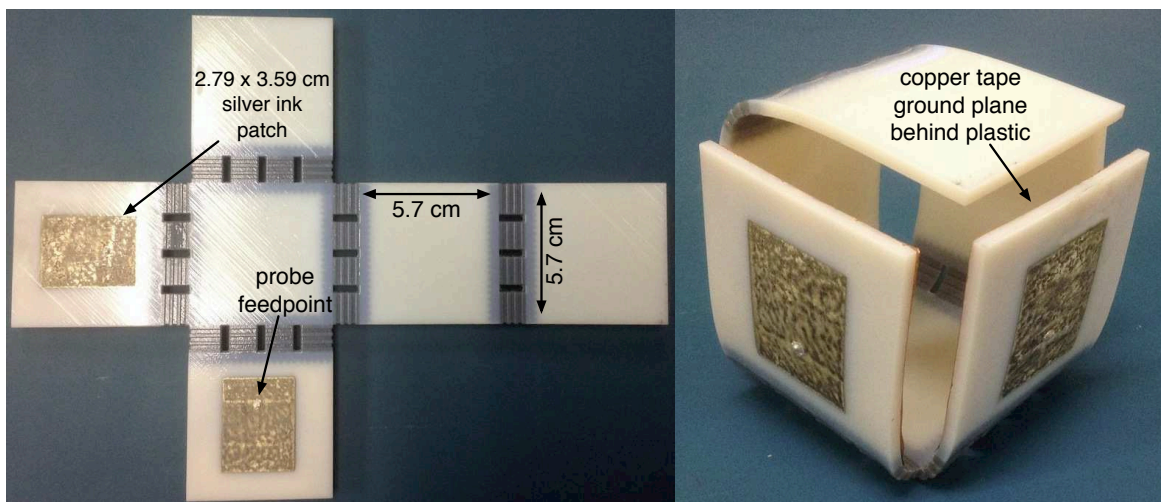
Fig. 14. Left: Inkjet-printed patch antenna on unfolded 3D-printed cube. Right: "Origami"-folded cube after heating, folding, and cooling down.
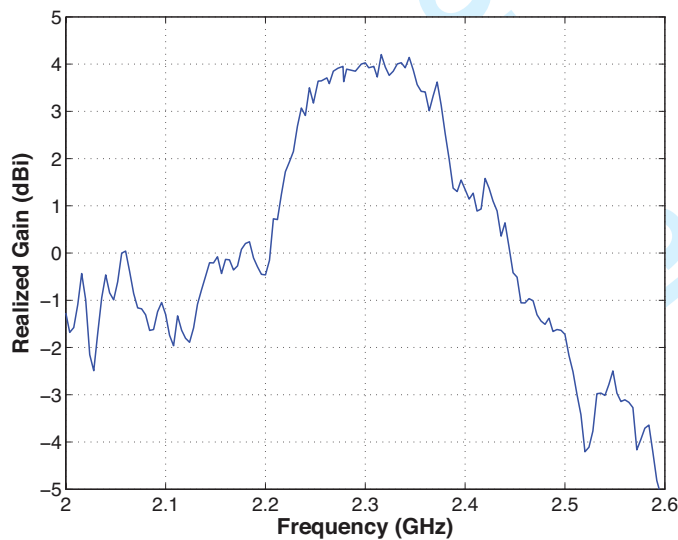

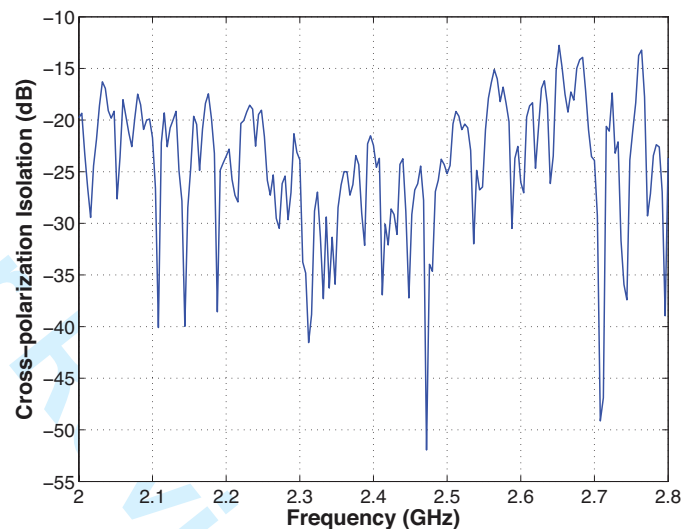Fig. 15. Measured realized gain of the inkjet-printed patch.

Fig. 16. Measured cross-polarization isolation of patch antenna.

the fabricated patch achieves gain values of up to $4 \sim 4.2$dBi at the resonance frequency.

The cross-polarization isolation (comparison between horizontal polarization field and vertical polarization field) is also measured by rotating the patch by $90°$ with respect to its center. As it is shown in Fig. 16, an isolation on the order of 25 dB or more is achieved in the $2.2 \sim 2.4$ GHz antenna operation band.

V. RF ENERGY HARVESTER DESIGN

As a proof-of-concept demonstration of utilizing additively manufactured origami structures for RF applications, a 2-port multi-direction RF energy harvester is designed, that exploits the independent inputs from the two orthogonal on-package antennas. The constraints for the design of a harvester for such a system are:

- The isolation between the two antennas is crucial, or else a far-field beam steering may occur for the total radiation pattern.
- The ability for the harvester to operate its two ports independently, without constraining both ports at the same time to a specific input power level, incoming signal frequency, and signal phase coherence.

The above constraints are addressed by using a DC-combining topology for the harvesting system, where each port has an individual RF-DC converter (rectifier) and the output voltage of the converters are combined to yield a higher voltage level. A DC combiner, in contrast with an RF-combining topology (e.g. an antenna array with a single RF feeding point), tends to "hide" the characteristics of the incoming RF signal at the DC output of each port's harvester. In that way, different input power/frequency/phase induced RF voltages are converted to DC voltages and combined to a single DC output.

To simplify the DC combining topology, the outputs of the two harvesters are directly connected at the load-driving terminal without any summation network utilizing resistors,
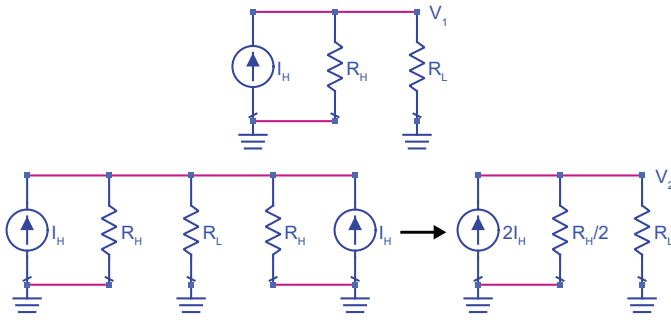
Fig. 17. Summation of two harvesters' outputs. Top: Single harvester source. Bottom: Two harvester sources and equivalent single-source circuit.

Fig. 18. Output voltage gain for 2 parallel harvesters compare to single harvester.

diodes, or field effect transistors (FETs). That way, the losses due to resistive elements or parasitics of the summation network are minimized. Without loss of generality, consider a single harvester represented as a current source (Norton equivalent) connected to a load R_L (Fig. 17-top). For a given input power P_{in} and frequency f, the harvester is able to output a current I_H and will feature an output impedance R_H. Then the voltage at the terminals of the load is

$$V_1 = I_H(R_L||R_H) = I_H \frac{R_L R_H}{R_L + R_H}. \quad (1)$$

When two harvesters excited with the same frequency and power level are connected in parallel (Fig. 17-bottom), the voltage at the terminals of the load is

$$V_2 = 2I_H(R_L||R_H/2) = 2I_H \frac{R_L R_H/2}{R_L + R_H/2} = I_H \frac{R_L R_H}{R_L + R_H/2}. \quad (2)$$

Comparing the two voltage levels V_1, V_2, the voltage gain for the 2-port harvester compared to a 1-port harvester is

$$\frac{V_2}{V_1} = \frac{R_L + R_H}{R_L + R_H/2}. \quad (3)$$

Asymptotically, the maximum voltage gain that can be achieved for equal power RF inputs is 2, which is anticipated. Fig. 18 shows the voltage gain for different load values and harvester equivalent output impedance values.

The 3D multi-direction harvester presented in this paper consists of two rectification circuits with their DC outputs combined at a single DC terminal that drives the load. Whether a voltage doubler topology or a single diode harvester topology is preferable has been determined through numerous simulations. One model for each case has been designed, based on full wave circuit board simulation, non-linear diode models, and lumped component models with parasitics. Both designs have been optimized for S-parameters tuning at the same frequency and input power level (2.3 GHz/ -15 dBm). However, while sweeping across different frequencies in the $2 \sim 2.6$ GHz band and power levels from -30 to 0 dBm, it has been noticed that in the case of the voltage doubler the resonance point occurs around 2.3 GHz with little or no shift for any power level. In contrast, for the single diode harvester, the resonance point will be strongly detuned in frequency depending on the power level. Thus, the voltage
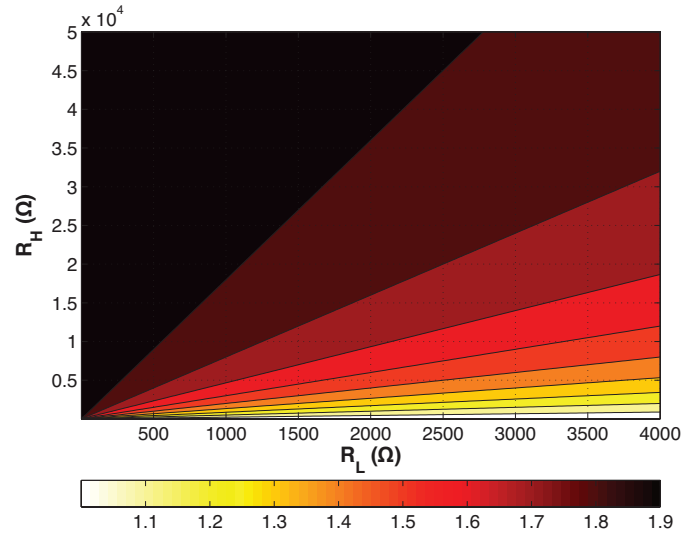
doubler topology is selected, since it can accommodate for small frequency shifts due to fabrication tolerances.

A single-stage voltage doubler is utilized for *each* antenna port, built with HSMS-285 zero-bias Schottky diodes (Fig. 19). At the output terminal, a large 0.22 μF DC capacitor is used for smoothing, along with a high-frequency 6.8 pF capacitor that operates below its self-resonance frequency, and thus is effective for smoothing high frequency signals. A small load of $R_L = 2$ KΩ is driven by the harvester output. Load values of this order of magnitude can be found in devices such as low-power microcontrollers that can be used for various WSN node implementations featuring sensors, backscatter communicators, etc.

The 2-port harvester has been designed and simulated with the Agilent Advanced Design System (ADS) software, using large signal S-parameters (LSSP) and harmonic balance (HB) simulations. Non-linear models have been utilized for the diodes, and the passive components have been simulated with models that include parasitics. The harvester has been implemented on a thin Rogers RO4003C laminate and can be seen in Fig. 20. The tuning of the ports at 2.3 GHz is performed with single stub matching networks that are implemented on the same board for minimizing losses due to connectors, and to minimize the total electronics' volume. Since the diodes utilized for harvesting typically show a high impedance (and thus mismatch) for low input power levels, the matching network was designed to maximize the power transfer from the antennas to the harvester in low power levels where no power could be compromised. The input power level of -15 dBm has been selected, at which, usable output voltage levels on the order of millivolts are achieved.

VI. HARVESTER MEASUREMENTS

The 2-port harvester prototype has been fully characterized using a VNA across the $2 \sim 2.6$ GHz band for power levels up to 0 dBm. The matching for both ports is optimal at -14.5 dBm RF input at each port, with both ports tuned
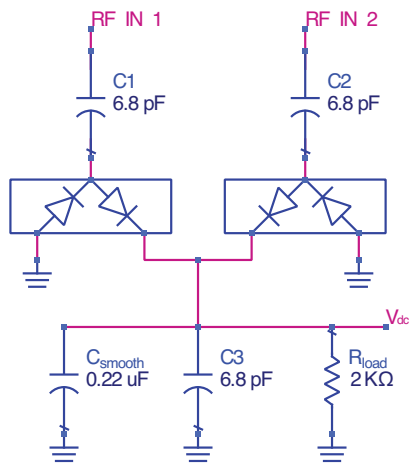
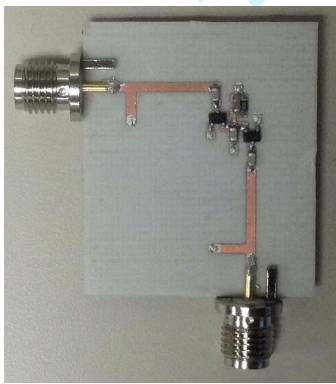Fig. 19. Schematic of the 2-port harvester with DC combining.

Fig. 20. Fabricated harvester prototype with on-board matching.

Fig. 21. Measured harvester ports' return loss and coupling (input power level: -14.5 dBm).

Fig. 22. Harvester port matching across frequency band and input power levels. Resonance around -14.5 dBm/2.3 GHz.

around 2.3 GHz, as it can be seen in Fig. 21. The -10 dB bandwidth is wider than 120 MHz and the ports show a slight resonant frequency difference between them. The isolation (insertion loss, IL) between the two ports is more than 45 dB over the entire bandwidth; the high RF isolation between the two ports, due to the DC connection point, guarantees the individual operation of the two harvesters regardless of the exact frequency and power level incident at each port.

In Fig. 22, the return loss of one of the harvester's ports is shown as a function of both the frequency and the power level of the incident wave on a contour plot. The resonant point at 2.3 GHz/-14.5 dBm can be clearly observed. Moreover, the "oval"-shaped contours centered centered around the resonant point show that for any given power level, the return loss minimum always occurs around 2.3 GHz, as discussed previously for the voltage doubler architecture.

In Fig. 23 it can be seen that across the whole frequency band and for any power level, the isolation between the two ports is always higher than 45 dB, with certain points reaching isolation values of 70 dB.

The device has been excited in three different scenarios to measure the output voltage: port 1 only, port 2 only, and both ports excitation. In Fig. 24, the simulated output voltage for different input power levels is shown, along with the measured values in these three scenarios. The wired measurements match
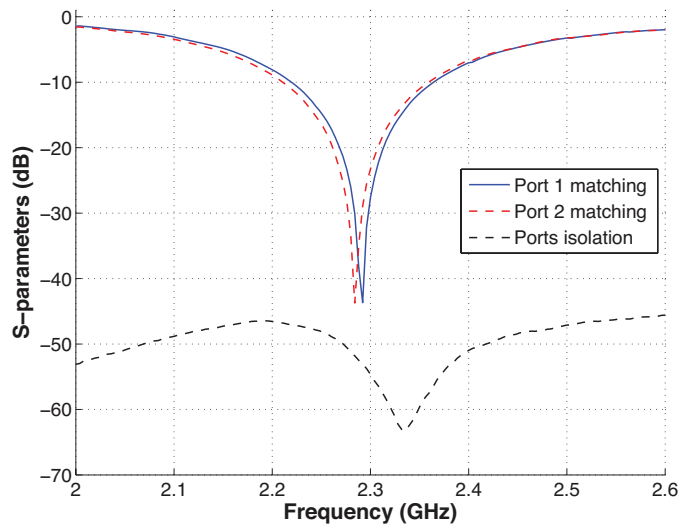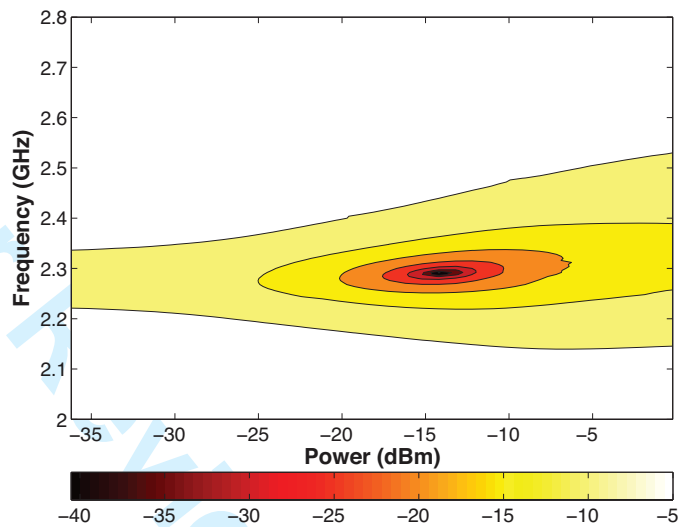
with the simulation results; as an example, at -15 dBm a voltage level of 100 mV is achieved for the 2 KΩ load when one port is excited. When both ports are excited, the voltage level is boosted to 150 mV. When the ports are excited with high power (0 dBm), the output voltage reaches 1.2 V, even though the harvester is not optimized for high input power operation.

VII. System Measurements

After characterizing the harvester and the packaging individually, everything is connected together for an evaluation of the final system. The electronics are placed inside the cube, connected to the patch antenna ports with short, flexible coaxial cables (Fig. 25). Since the cables are in close proximity inside the package, the coupling between them is measured in extreme scenarios, such as twisting the pair of RF cables together, or running them in parallel. In all cases, the coupling
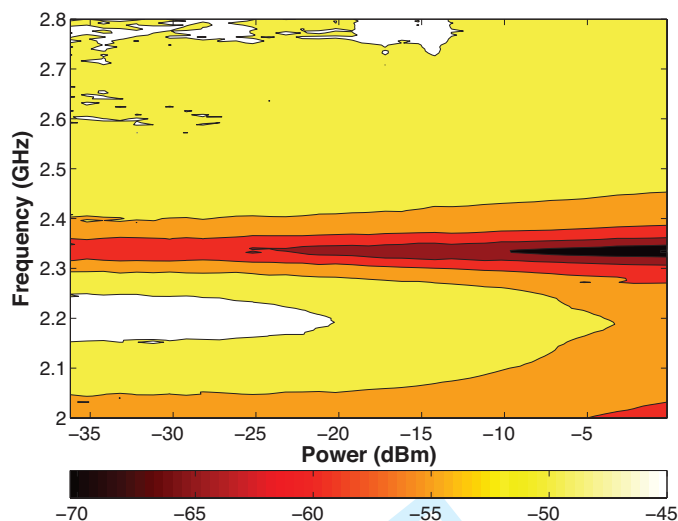
Fig. 23. Harvester port isolation across frequency band and input power levels. High isolation (more than 45 dB) for all points.
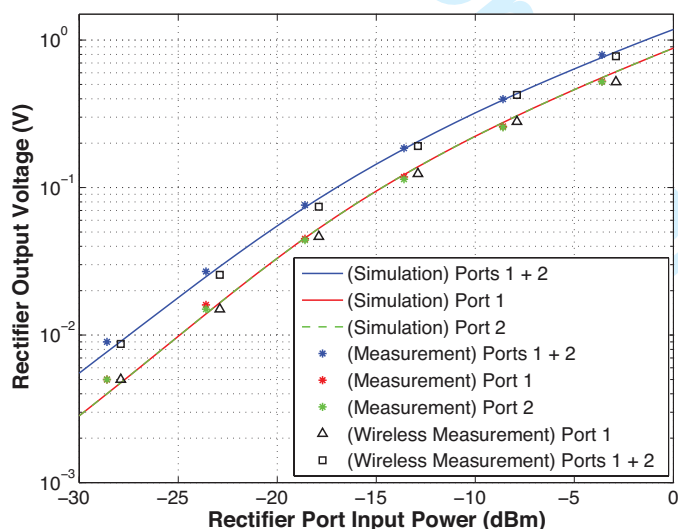

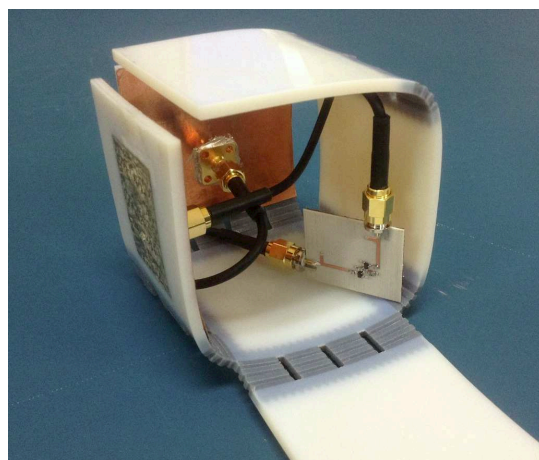Fig. 24. Harvester output voltage versus port input power.

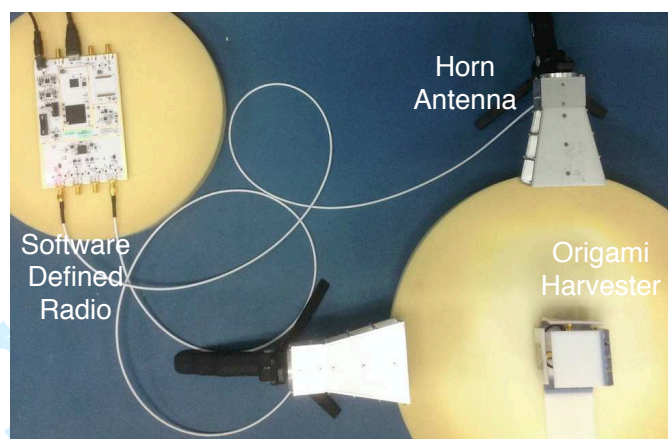Fig. 25. Origami package with harvester electronics inside.

Fig. 26. Wireless measurement setup for the origami RF harvester.

origami antennas, the output voltage has been recorded for each power level. The wireless measurements curve fits with the simulation and the wired measurements one, verifying the system operation with the inkjet-printed antenna on the 3D-printed, "origami"-folded cube (Fig. 24).

VIII. CONCLUSION - TECHNOLOGY POTENTIAL

In this paper, a full system has been presented to showcase the feasibility of utilizing origami-folding principles for high frequency applications. Additive manufacturing technology has been utilized to build a 3D package for RF electronics of a WSN node. Instead of fabricating the package in its 3D configuration, which would require considerable amounts of time and supporting material cost, a methodology of fabrication processes has been developed that significantly reduces the required fabrication time. Moreover, it effectively eliminates the need for supporting material, thus reducing the overall cost. The process involves the fabrication of a planar structure with 3D printing technology and subsequently utilizing inkjet printing to form conductors directly on its surface. The planar structure can then be folded to a 3D shape in an origami fashion by heat-activating its "smart" shape-memory hinges. As a proof-of-concept a full system has been built that fully

between the cables was lower than -70 dB, and no specific setup of the cables was required in the package to minimize cross-port interference.

A software-defined-radio (SDR) with tunable output power was set up to transmit a 2.3 GHz constant wave (CW) from two ports that were connected to two horn antennas. The horn antennas were chosen for their high directivity, to create plane waves at at specific directions in the far field, i.e. to eliminate any reflections from side- or back-lobes that could potentially excite both patch antennas instead of only the targeted one. The horn antennas were in an orthogonal configuration, to excite one patch each, and at the same distance, to keep path loss at similar levels (Fig. 26).

The inkjet-printed patches have been illuminated by the horn antennas at several power levels, while the power induced at each antenna's terminals has been monitored with an RF power meter to precisely monitor the input power to the harvester at each case. After connecting the harvester to the
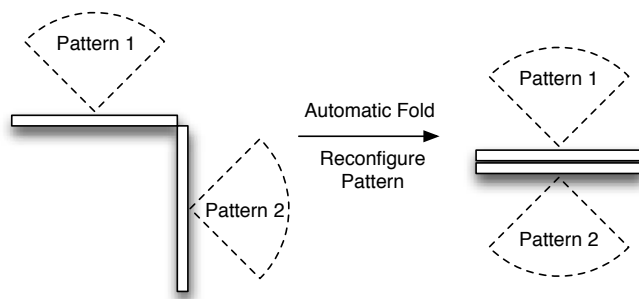
Fig. 27. Potential for origami technology: shape-changing structures for on-the-fly reconfigurable RF systems and smart wireless sensors.

utilizes the geometry of the 3D origami package for multi-direction high frequency energy harvesting. Inkjet-printed on-package antennas are effectively utilized to capture RF signals from orthogonal directions, which would not be otherwise possible with directional planar antennas. This work is a successful demonstration of combining 3D-printed origami and inkjet-printed RF structures for demanding high-frequency applications.

The potential of utilizing origami techniques for RF applications is not limited to packaging. The ability to change the shape of 3D structures opens new paths in electromagnetic applications. Apart from its direct benefits of reducing the required fabrication time and material cost by folding 2D shapes to 3D ones, the most significant benefit is the ability for reconfiguration. Shape-memory hinges can be built either to fold or unfold automatically, with heat triggering, and without manual force. This could enable complex structures to be reconfigured on-the-fly based on the ambient temperature conditions. In that case, smart sensors could be built, that signal rapid changes in temperature by changing their RF characteristics. An example could be directional antennas that change their radiation pattern when automatically folded (Fig. 27). In the same manner, reconfigurable antennas, transmission lines, filters, and numerous others RF structures could reconfigure their frequency of operation, gain, bandwidth, or phase. In a different approach, intentional changes of the temperature around the proximity of the system could enable the live, controlled reconfiguration by folding or unfolding the origami structure to tune, for example, a filter. Beam steering for small antenna arrays by physically changing their geometry without the need for servo motors or manual force could be appealing for low-cost applications. This work demonstrated the feasibility of incorporating origami for RF applications and the methodology presented to additively manufacture complex origami structures will be enabling the fabrication of numerous other systems for demanding, non-conventional electromagnetic applications.

REFERENCES

[1] S. Kim, R. Vyas, J. Bito, K. Niotaki, A. Collado, A. Georgiadis, and M. M. Tentzeris, "Ambient RF energy-harvesting technologies for self-sustainable standalone wireless sensor platforms," *Proc. IEEE*, vol. 102, no. 11, pp. 1649–1666, Nov. 2014.

[2] K. Gudan, S. Chemishkian, J. J. Hull, S. J. Thomas, J. Ensworth, and M. S. Reynolds, "A 2.4GHz ambient RF energy harvesting system with -20dBm minimum input power and NiMH battery storage," in *IEEE Int. Conf. on RFID-Technology and Applications (RFID-TA)*, Tampere, Finland, Sep. 2014, pp. 7–12.

[3] Y.-H. Suh and K. Chang, "A high-efficiency dual-frequency rectenna for 2.45-and 5.8-GHz wireless power transmission," *IEEE Trans. Microw. Theory Tech.*, vol. 50, no. 7, pp. 1784–1789, 2002.

[4] R. Scheeler, S. Korhummel, and Z. Popovic, "A dual-frequency ultralow-power efficient 0.5-g rectenna," *IEEE Microw. Mag.*, vol. 15, no. 1, pp. 109–114, 2014.

[5] D. Masotti, A. Costanzo, M. Del Prete, and V. Rizzoli, "Genetic-based design of a tetra-band high-efficiency radio-frequency energy harvesting system," *IET Microw,, Antennas & Propag.*, vol. 7, no. 15, pp. 1254–1263, 2013.

[6] Z. P. N.P. Basta, E.A. Falkenstein, "Bow-tie rectenna arrays," in *Proc. 2015 IEEE MTT-S Wireless Power Transfer Conf. (WPTC)*, Boulder, CO, May 2015.

[7] B. Strassner and K. Chang, "5.8-ghz circularly polarized dual-rhombic-loop traveling-wave rectifying antenna for low power-density wireless power transmission applications," *IEEE Trans. Microw. Theory Tech.*, vol. 51, no. 5, pp. 1548–1553, 2003.

[8] N. Shinohara and H. Matsumoto, "Experimental study of large rectenna array for microwave energy transmission," *IEEE Trans. Microw. Theory Tech.*, vol. 46, no. 3, pp. 261–268, 1998.

[9] Q. Ge, C. K. Dunn, H. J. Qi, and M. L. Dunn, "Active origami by 4D printing," *Smart Materials and Structures*, vol. 23, no. 9, p. 094007, 2014.

[10] J. Hester, S. Kim, J. Bito, T. Le, J. Kimionis, D. Revier, C. Saintsing, W. Su, B. Tehrani, A. Traille, B. Cook, and M. Tentzeris, "Additively manufactured nanotechnology and origami-enabled flexible microwave electronics," *Proc. IEEE*, vol. 103, no. 4, pp. 583–606, Apr. 2015.

[11] J. Kimionis, A. Georgiadis, M. Isakov, H. J. Qi, and M. M. Tentzeris, "3D/inkjet-printed origami antennas for multi-direction RF harvesting," in *IEEE MTT-S Int. Microwave Symp. (IMS)*, Phoenix, AZ, May 2015.

[12] H. J. Qi, T. D. Nguyen, F. Castro, C. M. Yakacki, and R. Shandas, "Finite deformation thermo-mechanical behavior of thermally induced shape memory polymers," *Journal of the Mechanics and Physics of Solids*, vol. 56, no. 5, pp. 1730–1751, 2008.

[13] Y. Li, N. Kaynia, S. Rudykh, and M. C. Boyce, "Wrinkling of interfacial layers in stratified composites," *Advanced Engineering Materials*, vol. 15, no. 10, pp. 921–926, 2013.

[14] B. Tehrani, B. S. Cook, and M. M. Tentzeris, "Post-process fabrication of multilayer mm-wave on-package antennas with inkjet printing," in *2015 IEEE Int. Symp. on Antennas and Propagat. (APSURSI)*, Vancouver, BC, Canada, Jul. 2015.

[15] R. Martinez, J. Kimionis, A. Georgiadis, A. Collado, M. Tentzeris, G. Goussetis, and J. Tornero, "Planar monopole antennas on substrates fabricated through an additive manufacturing process," in *9th European Conf. on Antennas and Propag. (EuCAP)*, Lisbon, Portugal, Apr. 2015.